Efficient electrophoretic deposition of MXene/reduced graphene oxide flexible electrodes for all-solid-state supercapacitors

Keliang Wang [a,b,*], Bocong Zheng [a,b], Madeline Mackinder [b], Nina Baule [a], Elias Garratt [a,b], Hong Jin [c,*], Thomas Schuelke [a,b], Qi Hua Fan [a,b,*]

[a] *Fraunhofer USA, Inc. Center for Coatings and Diamond Technologies, Michigan State University, East Lansing, MI 48824, USA*
[b] *Department of Electrical Engineering and Computer Engineering & Department of Chemical Engineering and Materials Science, Michigan State University, East Lansing, MI 48824, United States*
[c] *Suzhou Research Institute, Xi'an Jiaotong University, Suzhou 215123, People's Republic of China*

ABSTRACT

MXene has been considered as a promising electrode materials for energy storage devices. This work reports using an electrophoresis effect to efficiently deposit $Ti_3C_2T_x$/rGO composite on flexible substrates, which are subsequently used as the electrodes of all-solid-state supercapacitors. The electrophoresis deposition does not require a binder in the fabrication of the $Ti_3C_2T_x$/rGO electrodes. The structures and properties of the MXene/graphene electrode materials are characterized using Zeta potential, scanning electronic microscope, X-ray powder diffraction, Fourier-transform infrared and X-ray photoelectron spectroscopy. The performance of the all-solid-state flexible supercapacitors are evaluated using cyclic voltammetry, galvanostatic charge/discharge, electrochemical impedance spectroscopy, and cycle life tests. The devices show high areal specific capacitance of ~12 mF cm^{-2}, small resistance, and excellent cycling stability at different current densities for over 4,000 cycles. Moreover, the all-solid-state flexible supercapacitors exhibit superior mechanical flexibility under different deformations.

1. Introduction

The increasing demand for energy has become the top challenge to sustain the global economic growth [1–4]. Energy storage is a critical segment in the energy infrastructure. Lithium batteries and supercapacitors are the most important energy storage components for portable electronic devices and automobiles [5,6]. Supercapacitors are of particularly attractive for applications that require high power density, fast charge/discharge and outstanding cycling stability. Supercapacitors can be classified into pseudocapacitors and electrical double layer capacitors (EDLCs), based on the energy storage mechanisms. EDLCs have better stability as compared with pseudocapacitors due to direct ion adsorption/desorption during the charge and discharge [7,8]. Efforts in the past decades have been devoted to the research of supercapacitor electrode materials aiming to achieve excellent capacitance performance [4,9,10]. The recent advancement in lightweight portable and wearable electronic devices imposes a strong need for and subsequently intensive studies of all-solid-state flexible supercapacitors [11–13].

Carbon-based materials, including activated carbon derived from biomass, carbon nanotubes, carbon fibers, and graphene, are among the mostly reported all-solid-state EDLC electrodes [14–17]. Many strategies have been proposed to improve the capacitance performance, such as doping heteroatoms in the electrode materials to tune the electronic structures and electric conductivity [18,19], chemical and physical activation to increase the accessible surface areas and pore structures [20,21], and polymer modification to induce a pseudocapacitance behavior [22,23]. Although these strategies work well, further improvement in the performance of the electrode materials is still highly desirable. In 2011, Yury et al. discovered that the 2D structured MXene had superior stability and was a promising electrode material for EDLCs [24]. This type of new 2D materials have a general formula of $M_{n+1}X_nT_x$, where M is an early transition metal, X is carbon and/or nitrogen, and T_x is a surface functional termination (*e.g.* -OH, -F, or -O) [25]. As a result of their surface functional terminations and distinct architecture, MXenes could be hydrophilic in favor of ion transport with great potential for supercapacitors [26].

The electrode processing plays a critical role in determining the

---

performance of all-solid-state flexible supercapacitors. The reported methods for fabricating the electrodes include hydrothermal pressing, spray coating, and casting. These processes require expensive binder (~10 %) for linking the randomly oriented porous powder, leading to reduced overall specific capacitance and increased cost of the supercapacitors. The common binders, such as PTFE and PVDF, are fluorinated materials, which have recently caused serious health and environmental concerns. In addition, these processes include prolonged drying [27,28,29].

The present work demonstrates an efficient electrophoretic deposition (EPD) that overcomes the limitations of the existing methods for fabricating flexible electrodes of supercapacitors. Under a non-uniform electric field, polarized MXene/rGO composite exfoliated by a CH_4 plasma can be uniformly deposited onto a flexible carbon cloth, which acts as the current collector and flexible substrate. The electrophoretic process enables the MXene/rGO powders to densely pack in a way that significantly promotes the *Van der Waals* interactions. As a result, no binders are needed. The subsequently assembled all-solid-state supercapacitors present high specific capacitance, low series resistance, superior cycling stability, and excellent mechanical flexibility. Moreover, the electrophoretic deposition can be realized by a safe voltage of ~30 V in a MXene/rGO colloidal solution and the electrodes can be directly used for fabricating supercapacitors, greatly reducing the process time.

2. Experimental

All the chemicals and materials used in the experiments were as received from Fisher Scientific Inc. if not otherwise specified.

2.1. Preparation of graphite oxides

An improved Hummers' method [30] was used to prepare the graphite oxide (GO). A typical process follows. 2.5 g graphite flakes were mixed with 75 ml concentrated sulfuric acid (H_2SO_4, 98 *wt*%) under vigorous stirring in a cold bath around 0 °C for 4 h. Then, 1.25 g sodium nitrate ($NaNO_3$) and potassium permanganate ($KMnO_4$) were slowly added in sequence. After 12 h of reaction at room temperature, 25 mL deionized water was added into the mixture dropwise and the reaction temperature was increased to 98 °C gradually prior to adding an additional 75 mL deionized water. After 4 h, 7.5 mL hydrogen peroxide (H_2O_2, 30 *wt*%) was dropwise added and the suspension changed from black to yellow colloid. The colloid mixture was then transferred into several dialysis tubes (14,000 MWCO Daltons) to dialyze in deionized water for 7 days until the pH was close to 7. The dialyzed colloid solution was then stored in a refrigerator and denoted as GO.

2.2. Preparation of $Ti_3C_2T_x$

The MXene of $Ti_3C_2T_x$ was prepared by hydrofluoric acid (HF) etching as reported in [31]. A typical process follows. 1 g precursor of MAX phase Ti_3AlC_2 was dispersed into 10 mL HF (48 *wt*%) under vigorous stirring at room temperature for 24 h in a Polytetrafluoroethylene (PTFE) container. The suspension was then centrifuged at 4000 rpm for 5 min each time until the pH of the supernatant was close to 7. The sediment was collected and dried in an oven at 60 °C overnight. The prepared sample was denoted as $Ti_3C_2T_x$. Caution, the HF must be cautiously handled in fume hood with necessary personal protective equipment due to health and safety concern.

2.3. Preparation of $Ti_3C_2T_x/GO$

150 mg $Ti_3C_2T_x$ powder and 7.5 mL GO colloid solution were added into 50 mL deionized water. The mixture was then homogenized by a homogenizer (Pro25D, Pro Scientific Inc.) at a speed of 12,000 rpm for 120 s. Then, the dispersion was poured into Petri dishes (100 mm diameter × 15 mm height) and horizontally placed into a fume hood to

dry naturally. After drying, $Ti_3C_2T_x/GO$ composite sheet was obtained by peeling off from the Petri dishes. $Ti_3C_2T_x/GO$ composite sheet was then placed in a quartz tube vacuum reactor for plasma exfoliation. The reactor was filled with 100 sccm CH_4 gas and the pressure was maintained at 2 Torr. The sheet sample was exfoliated into fluffy powders with GO reduction, in a few seconds once the plasma excitation power was increased to 75 W. The obtained samples were denoted as $Ti_3C_2T_x/rGO$.

2.4. Fabrication of flexible $Ti_3C_2T_x/rGO$ electrodes

$Ti_3C_2T_x/rGO$ electrodes were prepared by an electrophoretic deposition method. The flexible substrates were cut from carbon cloth (CC, MPL, Fuel Cell Earth Inc.) into 2.5 × 1 (length × width) cm^2 and cleaned with ethanol, acetone, and distilled water in sequence followed by drying in an oven at 60 °C. The cleaned CC was then treated by oxygen plasma for 90 s under 75 W at a pressure of 2 Torr to improve the hydrophilicity and then the mass was weighed. 20 mg $Ti_3C_2T_x/rGO$ powder was dispersed into 40 mL deionized water followed by ultrasonication for 10 min to form a $Ti_3C_2T_x/rGO$ suspension. A CC substrate and a piece of copper with a larger size than that of CC were used as anode and cathode, respectively, being immersed into the $Ti_3C_2T_x/rGO$ suspension. A DC voltage of 30 V was applied to the electrodes for 10 min and the $Ti_3C_2T_x/rGO$ coated CC was obtained as electrodes after drying at 60 °C for 12 h. The average loading mass of the electrode materials was ~2.5 mg after weighing.

2.5. Fabrication of all-solid-state flexible supercapacitors

Polyvinyl alcohol-phosphoric acid (PVA-H_3PO_4) gel electrolyte was prepared for the all-solid-state flexible supercapacitors. A typical process follows. 2 g PVA was added into 20 mL deionized water and heated to 100 °C until a transparent solution was formed. Then, 2 g H_3PO_4 was dropwise added into the solution under vigorous stirring for 2 h after the temperature decreased to 85 °C. The obtained PVA-H_3PO_4 gel electrolyte was casted onto the surface of $Ti_3C_2T_x/rGO$ coated CC electrodes and cured overnight at room temperature. Then, a sandwich structure was formed by placing a pair of $Ti_3C_2T_x/rGO$ coated CC electrodes face to face. The edges were then sealed with silicon glue and the exposed CC was used for electric connection in the electrochemical measurements.

2.6. Physical characterization

The surface charge status of the electrode materials was characterized using a Zeta potential meter (Malvern Zetasizer Nano-ZS). The crystal structure of the samples was characterized by X-ray diffraction (XRD) (Rigaku Smartlab, Rigaku Americas, Inc. USA). The surface functional groups of the samples were investigated by Fourier Transformed Infrared (FTIR, FT/IR-4000 Series, JASCO) spectroscopy. The morphologies and structures were examined by a scanning electron microscope (SEM) (6610LV, JEOL, Japan) equipped with energy dispersive spectrum (EDS). X-ray photoelectron spectroscopy (XPS) was performed on an SSX-100 system (Surface Science Laboratories, Inc.) equipped with a monochromated Al K_α X-ray source.

2.7. Electrochemical characterization

All the electrochemical measurements, including cyclic voltammetry (CV) and electrochemical impedance spectroscopy (EIS), were performed using a potentiostat (PGSTAT128N, Metrohm). The charge/discharge stability was measured by a battery charge/discharge system (BTS series, NEWARE, China).

3. Results and discussion

The measured zeta potentials of $Ti_3C_2T_x$ and $Ti_3C_2T_x/rGO$ are shown

in Fig. 1a. It can be seen that the zeta potential of $Ti_3C_2T_x$/rGO significantly shifts to negative −45 mV from −15 mV of the $Ti_3C_2T_x$, indicating that rGO brings more electro-negative groups to $Ti_3C_2T_x$ after the plasma exfoliation. Such a significant improvement in surface charge implies a potentially stronger polarization of $Ti_3C_2T_x$/rGO than $Ti_3C_2T_x$ alone. The EPD configuration is illustrated in Fig. 1b, where the CC is set as anode with a smaller surface area than a cooper sheet cathode. Under the electric field, the polarized $Ti_3C_2T_x$/rGO particles are driven toward and subsequently deposited onto the CC substrate. It is worth noting that the size of the cathode should be sufficiently large to create a non-uniform electric field, which facilitates the drift of $Ti_3C_2T_x$/rGO powder. The digital photos of CC before and after $Ti_3C_2T_x$/rGO electrophoresis are illustrated in Fig. 1c, showing an obviously visible coating layer after EPD.

The morphology evolution from the parent MAX phase of Ti_3AlC_2 to exfoliated $Ti_3C_2T_x$/rGO is examined using SEM. The Ti_3AlC_2 presents a dense layer-like structure, as shown in Fig. 2a. After HF etching, space between the layers is opened due to the removal of the Al-atom layer (Fig. 2b), leaving behind a periodic 2D layered structure. This 2D layered structure facilitates the efficient transport of the electrolyte ions due to the short diffusion path and subsequently improves the capacitance performance. However, aggregation and stacking can occur during the drying process due to the strong *van der Wasls* interactions between the adjacent nanosheets. To reduce these irreversible effects, GO is used to modify the $Ti_3C_2T_x$ by plasma exfoliation. This idea is inspired by our previous work of graphene exfoliation by plasmas [33]. In Fig. 2c, it can be observed that the space between the layers is successfully filled with GO. After CH_4 plasma treatment, the $Ti_3C_2T_x$/GO sheets are exfoliated into powders due to the instant reduction of GO to rGO and simultaneous expansion of the generated oxygen. After the exfoliation, $Ti_3C_2T_x$ and reduced graphene appear as $Ti_3C_2T_x$/rGO composite pieces with a few layers (Fig. 2d).

The structures of Ti_3AlC_2, $Ti_3C_2T_x$, rGO and $Ti_3C_2T_x$/rGO are characterized by XRD. The characteristic peaks located at 9.4°, 18.9° for Ti_3AlC_2 are corresponding to (002) and (004) planes, respectively, as illustrated in Fig. 3, which matches well with the standard diffraction patterns (PDF card # 7551324). After HF etching, these peaks shift to 8.8° and 18.1°, respectively. Additionally, the sharp peaks located at 33.7°, 36.7°, 38.4°, 38.9°, 44.7°, and 52.0° corresponding to (100), (103), (008), (104), (106), (108) planes of Ti_3AlC_2, respectively, either vanish or evolve into broad bands in the diffraction patterns of $Ti_3C_2T_x$. These structural evolutions are attributed to an increased *c*-lattice parameter and the Al atoms being removal by HF etching, which are consistent with the observed morphology changes in SEM. For the diffraction patterns of rGO, a characteristic broad peak located at 24° is presented (the inset of Fig. 3a) and becomes inconspicuous after integration due to weak intensity in comparison with others. Together with the characteristic diffraction peaks of $Ti_3C_2T_x$. These results imply that the rGO is
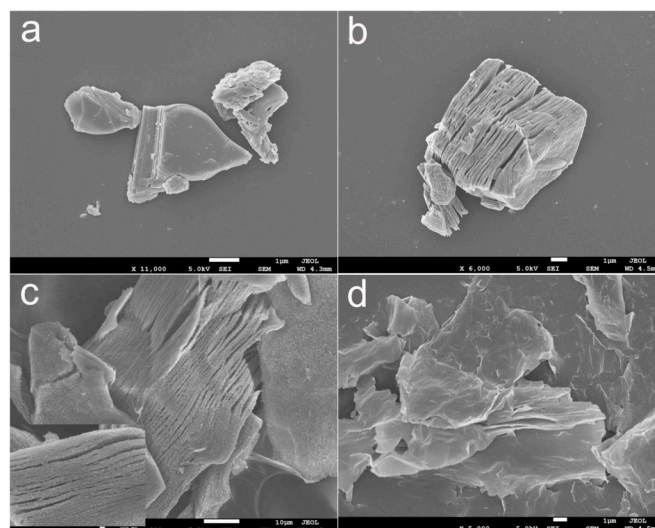
Fig. 2. SEM images of Ti_3AlC_2 (a), $Ti_3C_2T_x$ (b), $Ti_3C_2T_x$/GO (c) and $Ti_3C_2T_x$/rGO (d).

integrated in the skeleton of $Ti_3C_2T_x$ after CH_4 plasma exfoliation. XPS is then used to investigate the chemical composition of $Ti_3C_2T_x$/rGO (Fig. 3b). The element signals for C, Ti, O, and F are all detected but Al, further confirming the removal of Al atom layers and the introduction of potential F/O functional groups. The functional groups of GO, MXene and $Ti_3C_2T_x$/rGO are investigated by FTIR (Fig. S1). The peaks located at 2923, 1630, 1650 1120 cm^{-1} were attributed to —C—H, C=O, -OH, C—O, respectively, which showed up in all three sample. An inconspicuous peak at ~1100 cm^{-1} was presented was assigned to C-F bond for due to the etching. After modification, these hydrophilic functional groups would facilitate the wettability between electrode materials and electrolyte. The composition of $Ti_3C_2T_x$/rGO is determined to be 78.34 *at.*%, 17.27 *at.*%, 1.89 *at.*%, and 1.15 *at.*% for C, Ti, O, and F, respectively (the inset of Fig. 3b).

The morphologies of the CC substrates and $Ti_3C_2T_x$/rGO coated CC electrodes are examined using SEM (Fig. 4). The space in the CC substrate (Fig. 4a) are blocked, demonstrating the CC substrate is covered by densely packed $Ti_3C_2T_x$/rGO particles (Fig. 4b and c). Moreover, the deposited $Ti_3C_2T_x$/rGO are further confirmed in the cross-section measurement as shown in Fig. 4d. It is expected that the $Ti_3C_2T_x$/rGO particles are strongly polarized. During the electrophoresis process, an effective van der Waals force leads to electrostatic attractions between the particles. As a result, they tend to arrange closely to form a dense layer without the need of a binder. Further EDS and element mapping are carried out for CC (Fig. S2) and $Ti_3C_2T_x$/rGO coated CC (Fig. S3). C, O, and F are observed along the texture of the substrate for both samples

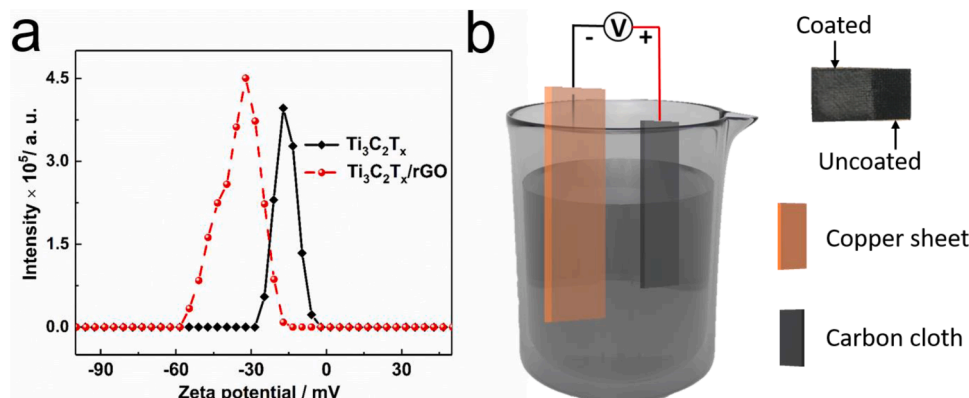**Fig. 1.** Zeta potential (a), schematic EPD set-up, and digital photos of CC and $Ti_3C_2T_x$/rGO coated CC (b).

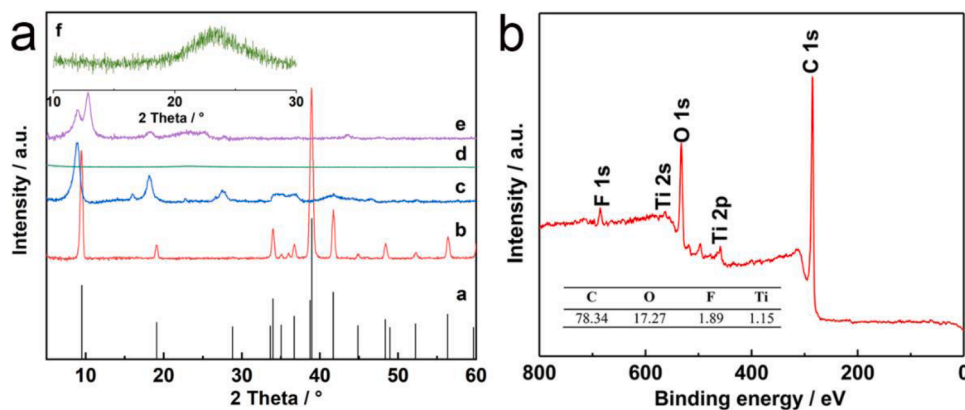**Fig. 3.** (a) XRD patterns of Ti₃AlC₂, Ti₃C₂Tₓ, Ti₃C₂Tₓ/rGO and XPS survey (b) of Ti₃C₂Tₓ/rGO. The inset is the atomic content of Ti₃C₂Tₓ/rGO.
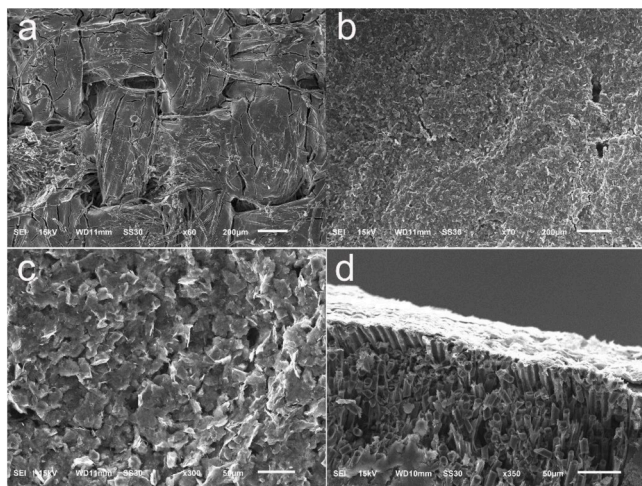

Fig. 4. SEM images of CC (a), Ti₃C₂Tₓ/rGO (b, c) and cross section of Ti₃C₂Tₓ/ rGO coated CC electrode (d).

and Ti is detected only in Ti₃C₂Tₓ/rGO coated CC. The EDS results are in consistent with the SEM. The signals of Si and F detected in the CC substrate might originate from the as-manufactured material and can be ignored.

The electrochemical performance of the fabricated all-solid-state flexible supercapacitors is verified by a variety of electrochemical characterizations, including CV, EIS and GCD. Fig. 5a shows the CV measurements at different scanning rates from 10 to 200 mV s⁻¹ in PVA-H₃PO₄. Quasi-rectangular shapes are observed for the Ti₃C₂Tₓ/rGO electrodes at scanning rates of 10, 20, 50, 100 and 200 mV s⁻¹, indicating the formation of electrochemical double layer and fast intercalation/de-intercalation of Ti₃C₂Tₓ/rGO electrode materials. To eliminate the potential capacitance impact coming from the pure CC, CV test at a scanning rate of 20 mV s⁻¹ is conducted for the devices with pure CC and Ti₃C₂Tₓ/rGO electrodes. The result is shown in Fig. S5, indicating a much smaller rectangular shape for pure CC than that of Ti₃C₂Tₓ/rGO. This result confirms that the capacitance contributed from CC is negligible. The GCD measurements are conducted to further characterize the capacitive performance. The Ti₃C₂Tₓ/rGO super-capacitors exhibit symmetric triangle charge-discharge curves at different current densities as shown in Fig. 5b, indicating excellent reversibility and capacitive characteristics of the electrodes. The areal specific capacitance of the device is determined from constant current charge/discharge curves using the following equation [32]:

$$C_A = \frac{2I \times \Delta t}{\Delta V \times S}$$

where C_A (F cm⁻²) is the areal specific capacitance, I (A) is the constant discharge current, Δt (s) is the discharge time, ΔV (V) is the potential window, and S (cm²) is the area of the electrodes. The calculated areal specific capacitances are 11.6, 9.0, 8.0 and 7.1 mF cm⁻² at current density of 0.1, 0.4, 0.6 and 0.8 mA cm⁻², respectively. The EIS measurements are conducted in a frequency range from 100 kHz to 0.01 Hz to evaluate the ion-transport behavior and electric resistance of the Ti₃C₂Tₓ/rGO electrode. As depicted in Fig. 5c, Ti₃C₂Tₓ/rGO electrodes present a typical capacitive-type impedance curve, consisting of an intercept, a semicircle and a spike in high, medium and low frequency ranges, respectively. The equivalent series resistance includes ohmic resistance (R_s), charger transfer resistance (R_{ct}) and *Warburg* impedance (W), which are related to the electrolyte, the contact between the electrolyte and electrode, and the structure of the electrode materials, respectively [34]. An equivalent circuit is simulated and displayed in the inset of Fig. 5c. In addition to the above elements, the capacitance (C_c) due to the contact interface and the capacitance (C_d) inside the pores are included [35,36]. The cycling stability of the fabricated device is also an important parameter to gauge the application potential. The cycle life tests are performed for over 4000 cycles at a series of current densities of 0.1, 0.4, 0.56 and 0.8 mA cm⁻². As shown in Fig. 5d, the areal specific capacitance gradually decreases as the charge/discharge current density increases. Almost 100% retention of capacitance is achieved for each individual 1000 cycles. In the extracted cycling between 2225 and 2245 (the inset of Fig. 5d), the GCD curves are symmetric triangles, indicating efficient sorption/desorption of the electrolyte ions and excellent reproducibility. It is worth noting that the areal specific capacitance recovers to the initial value of 11.6 mF cm⁻² at current density of 0.1 mA cm⁻² after 4000 cycles, which confirms the cycling stability of the electrode material and the corresponding supercapacitors.

Multiple devices connected in series and parallel are also studied to address the limits of the potential window and current density (Fig. 6). In CV tests at a scanning rate of 20 mV s⁻¹ and GCD tests at a current density of 0.1 mA cm⁻², the devices connected in series with two and three cells still exhibit rectangular and symmetrical triangle charge-discharge curves with extended potential window, respectively. When the devices are connected in parallel, rectangular and symmetrical triangle charge-discharge cures are observed as well in CV and GCD testes. These results indicate that good capacitance performance can be obtained using multiple devices, which offer the possibility for real applications in energy storage.

As flexible energy storage devices, the mechanical flexibility is essential. CV tests of the supercapacitors at 50 mV s⁻¹ are performed with different physical deformations (see optical images in Fig. 7) and the recorded curves are illustrated in Fig. 7. No obvious difference in the CV curves is observed when the device is bended over 90° or even twisted, indicating excellent flexibility of the supercapacitors.
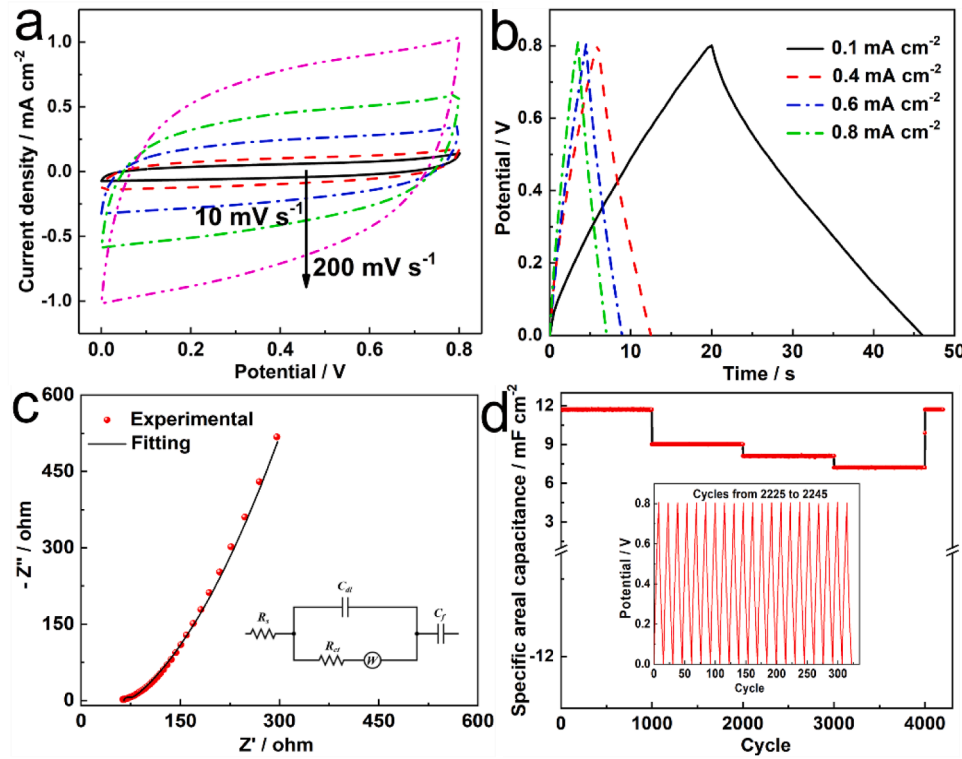
Fig. 5. CV (a) and galvanostatic charge/discharge (b) curves of Ti$_3$C$_2$T$_x$/rGO electrodes at different scanning rates and current densities, respectively; Nyquist plots (c) and life cycles (b) of Ti$_3$C$_2$T$_x$/rGO electrodes. The inset is partial test cycles.
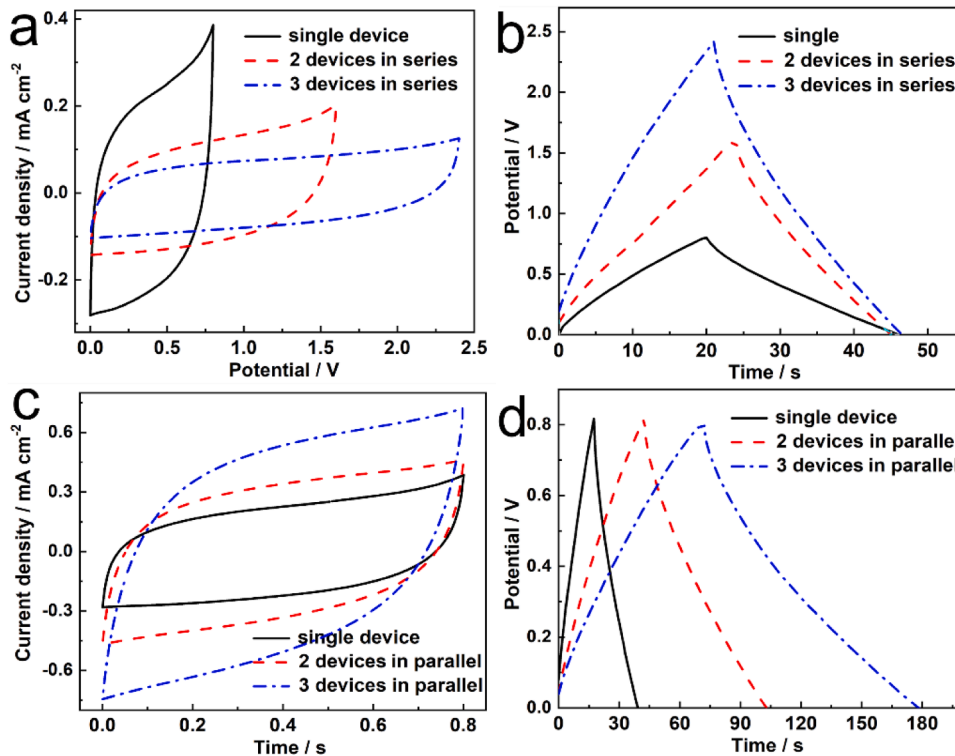

Fig. 6. CV (a, c) and galvanostatic charge/discharge curves (b, d) of one, two, and three devices in series and parallel, respectively.

4. Conclusion

Electrophoresis is an efficient method to deposit Ti$_3$C$_2$T$_x$/rGO onto carbon cloth and subsequently form flexible electrodes for all-solid-state supercapacitors. The electrophoretic deposition eliminates binders and greatly reduces the cost of the electrode materials. Plasma exfoliation forms layered Ti$_3$C$_2$T$_x$/rGO nanocomposite, in which the reduced GO also prevents the aggregation and stacking of Ti$_3$C$_2$T$_x$. The
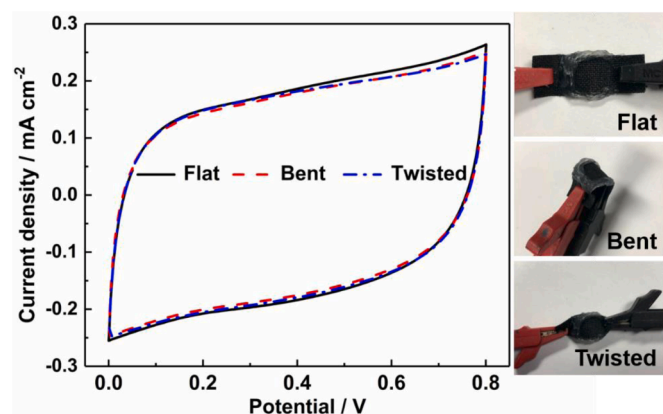
Fig. 7. CV curves of fabricated devices and optical images under deformation.

supercapacitors exhibit large areal capacitance of 11.6 mF cm^{-2} at 0.1 mA g^{-1} with small series resistance and excellent cycling stability. Multiple devices connected in series and parallel also exhibit stable capacitance performance with extended potential or current density ranges desirable for practical applications. Moreover, capacitance retention has been achieved for the flexible devices under external deformation.

Author statement

Keliang Wang designed and conducted experiments, summarized the data and wrote the manuscript. Bocong Zheng, Madeline Mackinder, Nina Baule and Elias Garratt helped in materials characterizations. Hong Jin, Thomas Schuelke and Qi Hua Fan revised the manuscript.

Declaration of Competing Interest

The authors declare that they have no known competing financial interests or personal relationships that could have appeared to influence the work reported in this paper.

Acknowledgment

Supplementary materials

Supplementary material associated with this article can be found, in the online version, at doi:10.1016/j.est.2020.102070.

References

[1] A.G. Pandolfo, A.F. Hollenkamp, J. Power Sources 157 (2006) 11–27.
[2] M. Aneke, M. Wang, Appl. Energy 179 (2016) 350–377.
[3] P. Simon, Y. Gogotsi, Nanoscience and Technology: a Collection of Reviews from Nature Journals, World Scientific, 2010, pp. 320–329.
[4] Z. Yu, L. Tetard, L. Zhai, J. Thomas, Energy Environ. Sci. 8 (2015) 702–730.
[5] C. Zhong, Y. Deng, W. Hu, J. Qiao, L. Zhang, J. Zhang, Chem. Soc. Rev. 44 (2015) 7484–7539.
[6] A. Rosenman, E. Markevich, G. Salitra, D. Aurbach, A. Garsuch, F.F. Chesneau, Adv. Energy Mater. 5 (2015), 1500212.
[7] C. Zhao, W. Zheng, Front. Energy Res. 3 (2015) 23.
[8] Y. Liu, X. Peng, Appl. Mater. Today 8 (2017) 104–115.
[9] A. González, E. Goikolea, J.A. Barrena, R. Mysyk, Renew. Sustain. Energy Rev. 58 (2016) 1189–1206.
[10] A. Borenstein, O. Hanna, R. Attias, S. Luski, T. Brousse, D. Aurbach, J. Mater. Chem. A 5 (2017) 12653–12672.
[11] Y.-Z. Zhang, Y. Wang, T. Cheng, W.-Y. Lai, H. Pang, W. Huang, Chem. Soc. Rev. 44 (2015) 5181–5199.
[12] L. Wen, F. Li, H.-M. Cheng, Adv. Mater. 28 (2016) 4306–4337.
[13] L. Dong, C. Xu, Y. Li, Z.-H. Huang, F. Kang, Q.-H. Yang, X. Zhao, J. Mater. Chem. A 4 (2016) 4659–4685.
[14] Z. Xiong, C. Liao, W. Han, X. Wang, Adv. Mater. 27 (2015) 4469–4475.
[15] D. Yu, S. Zhai, W. Jiang, K. Goh, L. Wei, X. Chen, R. Jiang, Y. Chen, Adv. Mater. 27 (2015) 4895–4901.
[16] Y. Chen, L. Du, P. Yang, P. Sun, X. Yu, W. Mai, J. Power Sources 287 (2015) 68–74.
[17] Z. Ling, Z. Wang, M. Zhang, C. Yu, G. Wang, Y. Dong, S. Liu, Y. Wang, J. Qiu, Adv. Funct. Mater. 26 (2016) 111–119.
[18] Y. Zhou, R. Ma, S.L. Candelaria, J. Wang, Q. Liu, E. Uchaker, P. Li, Y. Chen, G. Cao, J. Power Sources 314 (2016) 39–48.
[19] Y. Cheng, L. Huang, X. Xiao, B. Yao, L. Yuan, T. Li, Z. Hu, B. Wang, J. Wan, J. Zhou, Nano Energy 15 (2015) 66–74.
[20] W.-H. Qu, Y.-Y. Xu, A.-H. Lu, X.-Q. Zhang, W.-C. Li, Bioresour. Technol. 189 (2015) 285–291.
[21] C. Ma, X. Chen, D. Long, J. Wang, W. Qiao, L. Ling, Carbon 118 (2017) 699–708.
[22] Y. Liu, J. Zhou, J. Tang, W. Tang, Chem. Mater. 27 (2015) 7034–7041.
[23] X. Zang, S. Li, M. Zhu, X. Li, Z. Zhen, Y. He, K. Wang, J. Wei, F. Kang, H. Zhu, Nanoscale 7 (2015) 7318–7322.
[24] M. Naguib, M. Kurtoglu, V. Presser, J. Lu, J. Niu, M. Heon, L. Hultman, Y. Gogotsi, M.W. Barsoum, Adv. Mater. 23 (2011) 4248–4253.
[25] M. Naguib, V.N. Mochalin, M.W. Barsoum, Y. Gogotsi, Adv. Mater. 26 (2014) 992–1005.
[26] M. Hu, Z. Li, G. Li, T. Hu, C. Zhang, X. Wang, Adv. Mater. Technol. 2 (2017), 1700143.
[27] E. Ghoniem, S. Mori, A. Abdel-Moniem, J. Power Sources 324 (2016) 272–281.
[28] J. Wang, X. Li, Y. Zi, S. Wang, Z. Li, L. Zheng, F. Yi, S. Li, Z.L. Wang, Adv. Mater. 27 (2015) 4830–4836.
[29] L. Wang, H. Yang, X. Liu, R. Zeng, M. Li, Y. Huang, X. Hu, Angew. Chem. Int. Ed. 56 (2017) 1105–1110.
[30] W.S. Hummers Jr., R.E. Offeman, J. Am. Chem. Soc. 80 (1958) 1339.
[31] B. Anasori, M.R. Lukatskaya, Y. Gogotsi, Nat. Rev. Mater. 2 (2017) 16098.
[32] Y. Yang, Q. Huang, L. Niu, D. Wang, C. Yan, Y. She, Z. Zheng, Adv. Mater. 29 (2017), 1606679.
[33] K. Wang, B. Zheng, M. Shrestha, T. Schuelke, Q.-H. Fan, Energy Storage Mater. 14 (2018) 230–237.
[34] T. Zhu, J. Zhou, Z. Li, S. Li, W. Si, S. Zhuo, J. Mater. Chem. A 2 (2014) 12545–12551.
[35] C.-W. Huang, C.-H. Hsu, P.-L. Kuo, C.-T. Hsieh, H. Teng, Carbon 49 (2011) 895–903.
[36] C.-W. Huang, C.-M. Chuang, J.-M. Ting, H. Teng, J. Power Sources 183 (2008) 406–410.